Microfluid Nanofluid
DOI 10.1007/s10404-013-1184-y

RESEARCH PAPER

Flow rate analysis of an EWOD-based device: how important are wetting-line pinning and velocity effects?

Roxana Shabani · Hyoung J. Cho

Received: 11 January 2013 / Accepted: 3 April 2013

Abstract An electrowetting on dielectric (EWOD)-based micropump was used as a platform to study the contribution of the pinning and wetting-line velocity effects on its flow rate. In this micropump, a droplet is driven into a microchannel using EWOD to manipulate a meniscus in the channel. An interesting observation was that the shrinking input droplet changes its shape in two modes: (1) in the first mode, droplet contact angle decreases while its wetting area remains constant (pinning) and (2) in the second mode, droplet wetting line recedes while its contact angle changes as a function of its velocity (dynamic contact angle). Unexpectedly, the micropump flow rate was found to be constant in spite of the changes in the droplet radius. The pump performance was studied to unravel the physical concept behind its constant flow rate. A detailed characterization of variation in contact angle due to pinning, wetting-line velocity, and EWOD was carried out. Dynamic contact angles were used to accurately calculate the pressure gradient between the droplet and the meniscus for flow rate estimation. It was shown that neglecting either the wetting-line energy or the velocity effect results in not only a considerable gap between the predicted and the measured flow rates but also an unphysical instability in flow rate analysis. However, when these effects were fully taken into account, an excellent agreement between the predicted and the measured flow rates was obtained.

R. Shabani · H. J. Cho (✉)
Department of Mechanical and Aerospace Engineering, University of Central Florida, Orlando, FL 32816-2450, USA
e-mail: hjcho@ucf.edu

H. J. Cho
School of Advanced Materials Science and Engineering, Sungkyunkwan University, Suwon 440-746, Korea

Keywords Droplet · Electrowetting on dielectric · Hysteresis · Dynamic contact angle · Wetting-line velocity · Pinning · Advancing and receding wetting-lines

Abbreviations

EW	Electrowetting
EWOD	Electrowetting on dielectric
PDMS	Polydimethylsiloxane
SOG	Spin-on glass
WL	Wetting-line
WLE	Wetting-line energy
WLV	Wetting-line velocity

1 Introduction

In devices that are designed based on electrowetting on dielectric (EWOD), a liquid meniscus is manipulated by an applied voltage which reduces the contact angle of the wetting line (WL) formed at the boundary between the liquid, air, and the solid surface. The behavior of the moving WL has a complex nature due to the WL pinning and wetting-line velocity (WLV) effects, which alter the liquid contact angle on the solid surface from its equilibrium value obtained from Young's equation (Young 1805; Baviere et al. 2008). The wetting-line energy (WLE) effect or pinning effect is a result of the local microscopic defects on the solid surface (Tadmor 2004), by which liquid is pinned to the surface. Therefore, different values for contact angle are expected depending on whether the WL is in advancing or receding modes. The contact angle is also changed when the WL is moving, depending on the magnitude and direction of the WLV (Dussan 1979; Nelson et al. 2011). Theoretical and numerical models have been

Published online: 21 April 2013

developed to describe the moving WL (Shikhmurzaev 2006; Blake and De Coninck 2002; Huh and Scriven 1971); (Tanner 1979). In devices based on EWOD, the problem is more complicated due to the saturation of contact angle at higher voltages (Quinn et al. 2005; Mugele and Baret 2005). The study on the moving WL in electrowetting (EW)-based devices, for discrete droplet manipulation, has also been the focus of many studies (Zeng and Korsmeyer 2004; Berthier et al. 2007; Lu et al. 2007; Lienemann et al. 2006; Walker and Shapiro 2006; Walker et al. 2009; Jang et al. 2007; Ahmadi et al. 2010; Bahadur and Garimella 2006; Ren et al. 2002; Keshavarz-Motamed et al. 2009; Chen and Hsieh 2006; Schertzer et al. 2010). It has been shown that consideration of the pinning effect is essential to predict the accurate timescale of the droplet motion (Walker et al. 2009; Walker and Shapiro 2006). The dynamics of the WL was also investigated to model the droplet motion on the electrodes (Keshavarz-Motamed et al. 2009; Ren et al. 2002; Bahadur and Garimella 2006; Chen and Hsieh 2006; Sen and Kim 2009; Annapragada et al. 2011).

In this work, a combined theoretical/experimental approach was developed to study a continuous constant flow of an EWOD-based micropump. The flow was induced by manipulating a meniscus on an EWOD substrate, which corresponds to the bottom wall of a microchannel cast in a PDMS slab. An input droplet was used as a positive pressure source. By applying the voltage, the contact angle is reduced at the bottom of the channel, which results in a lower Laplace pressure inside the channel. Therefore, a positive pressure gradient is produced between the droplet and the meniscus. The droplet's WL recedes as it shrinks into an orifice leading to the channel. The WL pinning and the WLV effects need to be taken into account to describe the dynamic contact angles at the WLs: (1) the droplet's receding WL, (2) the advancing WLs of the liquid meniscus on the upper and side walls of the channel, and (3) the advancing WL on the bottom of the channel with a reduced contact angle due to EWOD. These two effects are crucial to developing a physically relevant model for the flow rate analysis. This is due to the fact that the accurate estimation of the contact angles is necessary to calculate the induced droplet/meniscus pressure gradient (Lu et al. 2007) and subsequently the micropump's flow rate.

2 Experiments and flow rate analysis

2.1 Contact angle hysteresis and mode switch

The EWOD substrate of the micropump consists of a silicon wafer spin-coated with a stack of three thin films of (1) polydimethylsiloxane (PDMS), (2) spin-on glass (SOG), and (3) a second layer of PDMS (Fig. 1). Silicon wafer is a conductive layer. SOG is an insulating layer with a thickness of 0.2 μm and a dielectric constant of 3.9 (Pai 1987; Wang et al. 1997). The first PDMS layer (on silicon) was found to improve the quality of the insulating layer by covering the surface defects. The second PDMS layer is used as a hydrophobic layer with a thickness of 1.1 μm. SU-8 mold on a different silicon wafer was used to cast a microchannel in a PDMS slab (soft lithography). The PDMS slab was bonded to the EWOD substrate to form a closed channel. A syringe pump was connected to the microchannel as shown in Fig. 1. The liquid flowed through the channel and then through a via-hole which has a bigger cross section compared to the channel, forming a droplet on the top of the orifice. The micropump's input droplet is stable with a contact angle of 86°. Only after applying a DC voltage between the silicon wafer and the steel pin (electrodes), the liquid will flow through the channel.

The input droplet is driven into the channel in two phases. In phase I, the droplet's wetting area remains constant until droplet's contact angle decreases to 80° due to pinning. Such phenomenon has been also observed for a passive micropump (Berthier and Beebe 2007). In contrast, in phase II, both the droplet's wetting area and contact angle decrease as the droplet is driven into the channel. The further decrease in droplet's contact angle is due to WLV effect (Shabani and Cho 2011). The reported variable droplet's contact angle on untreated PDMS surface is in agreement with the data reported in literature (Berthier and Beebe 2007; Shabani and Cho 2011). These results are later incorporated in the analysis of the micropump constant flow rate.

In an experiment, this phenomenon was studied for droplets with advancing and receding WLs by measuring the droplet's contact angle, θ_D, with respect to its WL

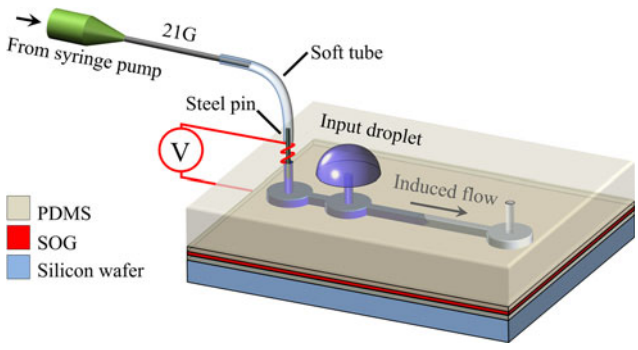

Fig. 1 EWOD-based micropump: a microchannel cast in PDMS slab is bonded to the EWOD substrate (PDMS/SOG/PDMS/Si). An input droplet is driven into the channel, and a continuous constant flow is induced upon turning on the voltage

position. A syringe pump was connected to a microchannel leading to an open orifice formed in a PDMS layer (Fig. 2a). Pinning without EWOD was observed by injecting (drawing) liquid at a very low flow rate to form an advancing (receding) droplet on the top of the orifice.

In stage 1 of the experiment, the liquid was pumped out of the orifice with a uniform and low flow rate of 0.1 μL/min (Fig. 3a). The contact angle remained constant at the advancing contact angle, θ_A, with an average of 86° as the WL was moving forward. In stage 2 the droplet from stage 1 was drawn back into the orifice using refilling mode of the syringe pump. The WL was pinned to the substrate as the contact angle was decreasing from θ_A to the receding contact angle, θ_R, with an average of 69°. In stage 3, the droplet was drawn further. The droplet contact angle remained constant at θ_R as the WL was receding. Then liquid was pumped out again (stage 4), and the droplet contact angle increased from θ_R to θ_A while the WL was pinned to the surface.

The contact angle hysteresis with four modes is shown as a closed loop by plotting the contact angle versus WL position (Fig. 3b). Droplet's WL position was measured from the center of the droplet. Interestingly, when EWOD is performed, the droplet exhibits a similar behavior, and only the contact angle hysteresis loop is shifted toward lower contact angles (Fig. 3b).

A high-gauge needle connected to a syringe pump was placed parallel to EWOD substrate (Si as lower electrode/dielectric SOG/hydrophobic PDMS) and used for injecting (drawing) liquid (Fig. 2b). The needle was also used as the upper electrode. A power supply was connected between the needle and the silicon substrate. Liquid was injected

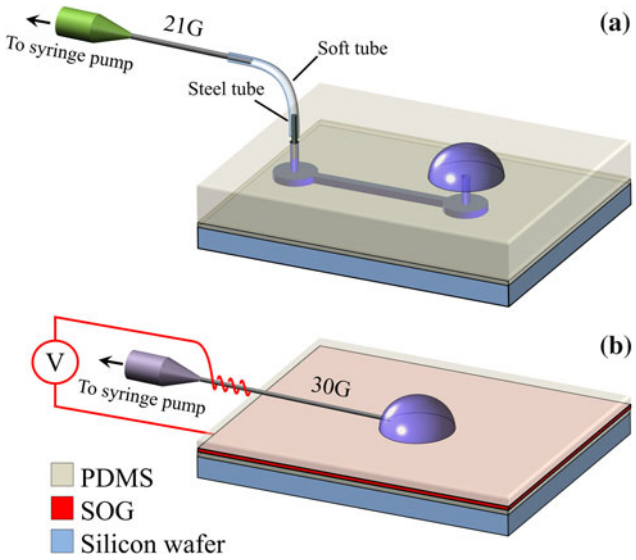

Fig. 2 Experimental setups for **a** contact angle hysteresis and wetting-line velocity effect without EWOD and **b** pinning effect with EWOD

(drawn) through the needle at a very low flow rate to form an advancing (receding) droplet on EWOD substrate. Contact angle hysteresis is reduced by increasing the DC voltage, as evidenced by the smaller area occupied by the hysteresis loop. This is discussed in more detail in the next section.

2.2 Wetting-line velocity effect

The advancing (receding) contact angles are further changed by the direction and the magnitude of the droplet's WLV (Dussan 1979; Blake 2006). In the next experiment this effect was shown for positive (advancing), zero, and negative (receding) velocities (Fig. 4a, b). The setup depicted in Fig. 2a was used to observe the effect of WLV on droplet contact angle by increasing the injecting (drawing) flow rate (dynamic contact angles). The contact angle was measured versus the WLV using frame-by-frame video analysis.

In stage A, a droplet is pumped out of the orifice (positive WL velocities). For a constant pumping rate, the droplet's WLV is higher when it is small and becomes

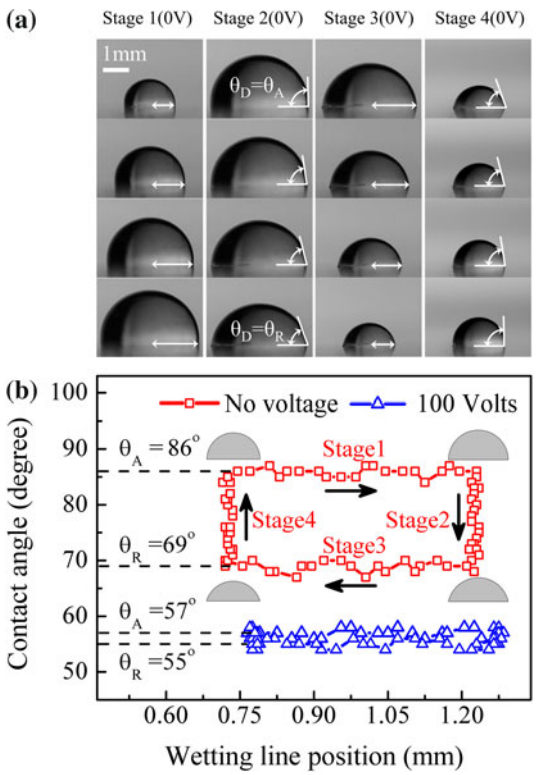

Fig. 3 Contact angle hysteresis and the mode switch. **a** A droplet (on the top of an orifice formed in PDMS) with advancing (stage 1), receding (stage 3), and pinned (stages 2 and 4) WLs when no voltage is applied. Droplet contact angle, θ_D, decreases in stage 2 and increases in stage 4 due to pinning. **b** Droplet contact angle versus its WL position, measured from the center of the droplet. Contact angle hysteresis loops for 0 and 100 V

lower for larger size of the droplet. A higher value for contact angle is observed for higher velocities.

In stage B, the droplet is drawn back into the orifice without giving time to the droplet for relaxation. The contact angle is reduced to 80°, while the wetted area remains constant. The contact angle change at zero velocity (vertical line) represents the pinning or the hysteresis in contact angle (Fig. 4b, stage B). In stage C, the droplet is drawn further resulting in negative WLV. Here, a smaller contact angle is observed for higher magnitude of the WL

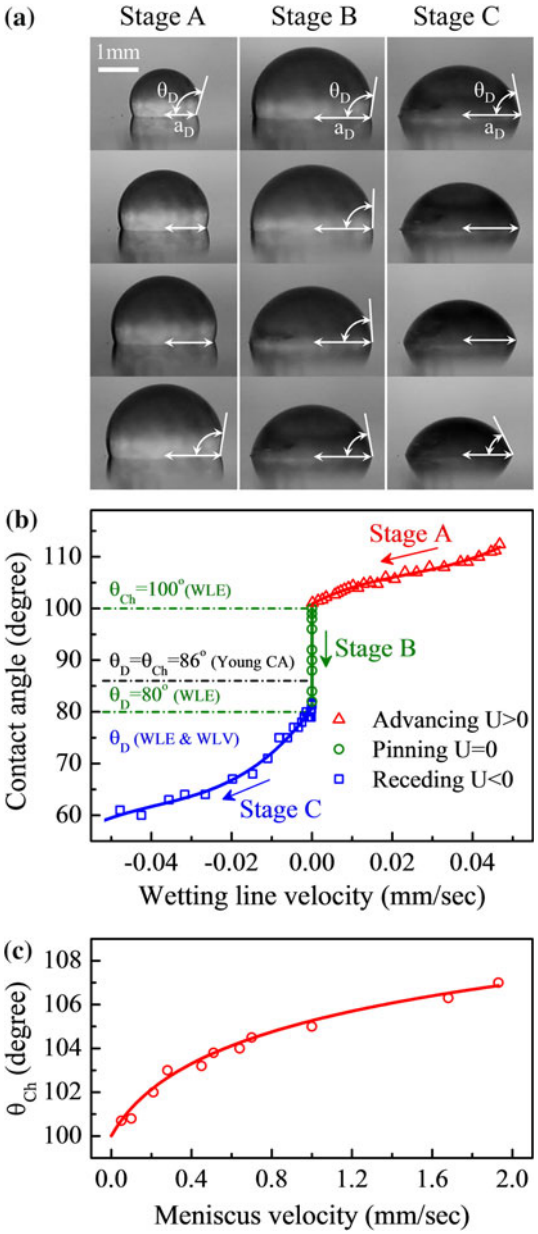

Fig. 4 WLV effect on the contact angle **a** droplet is pumped out (stage A) and drawn into (stages B and C) an orifice on PDMS surface. **b** Droplet dynamic contact angle versus its WLV. θ_D and θ_{Ch} used in models 1–3 are estimated and labeled. **c** Dynamic contact angle versus meniscus velocity in the channel

negative velocity. In summary, a significant change in contact angle as large as 50° could be induced by WLV and pinning effects for the range of WL velocities studied here. Measurement data for the receding WL are used (Fig. 4b, stage C) to describe the variable contact angle of the shrinking droplet versus its WLV during phase II of the micropump operation (Shabani and Cho 2011).

For an initial input droplet diameter of 1 mm, a meniscus velocity of 0.5 mm/sec was measured in the microchannel using frame-by-frame video analysis of the top view of an advancing meniscus in the channel. The liquid velocity was obtained from the slope of the measured meniscus position versus time. The meniscus velocity is much larger than the velocity of the droplet WL in Fig. 4b (<0.05 mm/sec).

For such high velocities the method used in Fig. 4a, b is not feasible due to limitation in flow rate of the syringe pump and the droplet instability and deformation in test setup of Fig. 2a. Fortunately, without applying any voltage to the setup depicted in Fig. 1, all four walls of the channel have the same contact angle and θ_{Ch} could be directly measured from top-view images. Meniscus velocities, U_{Ch}, as high as 2 mm/sec, could be easily achieved inside the channel (Fig. 4c). Experimental data depicted in Fig. 4c are used for the contact angle on the side and top walls of the channel in the flow rate analysis.

The last data needed are the liquid contact angle on the bottom of the channel, θ_{EW}, upon applying a DC voltage of 100 V. However, the direct observation of θ_{EW} from the side view of the PDMS channel is not feasible unlike the observation of θ_{Ch} from the top view. This is due to non-smooth and opaque surfaces when PDMS was cut on the sides. Moreover, the contact angle calculated by Young–Lippmann's equation for a voltage of 100 V could not be used since the pinning and WLV effect are present at the bottom of the channel (dynamic θ_{EW} at the advancing WL in the channel). Instead, θ_{EW} was considered as a fitting parameter, and the validity of the values obtained for θ_{EW} was justified by comparing with other experimental data, that is, the contact angle should be smaller in the presence of EWOD as compared to θ_{Ch}.

2.3 Derivation of governing equations for flow rate analysis

A novel approach for flow rate analysis is introduced by taking a dynamic contact angle into account in writing energy equation for the system. This is an improvement over sophisticated commercial software, limited only to equilibrium Young contact angle (Zeng and Korsmeyer 2004) based on Young's equation.

Here we need to highlight that (a) the flow rate inside the channel is a function of the meniscus contact angle and

(b) the contact angles themselves are a function of the flow rate. Therefore, a self-consistent solution could be obtained only using implicit computational methods.

The algorithm for this approach is developed following the continuity and energy equations, and its physical implications are demonstrated. The proposed algorithm could be fitted to various microfluidic systems with different geometries for flow rate estimation. A numerical calculation was carried out using MATLAB. Some of the parameters used in the analysis are shown in the side and top views of the micropump schematic (Fig. 5a, b). The size of the channel is exaggerated as compared to the orifice size, d, for clarity. The micropump channel has a rectangular cross section with a height, h, and a width, w (60 μm × 250 μm). Although the nominal depth of the channel is supposed to be 100 μm according to the data sheet provided by the SU-8 photoresist manufacturer (MicroChem Corp.), the channel thickness was measured at several different points using a surface profiler (Tencor Alpha-Step 200) to be 60 μm. The input droplet has a radius of curvature of R_D and a contact angle of θ_D. The liquid meniscus contact angles on the channel sides and top, θ_{Ch}, are similar, while the meniscus contact angle on the bottom of the channel, θ_{EW}, is smaller due to EWOD.

Also, the forces exerted on the meniscus WLs on the four walls of the channel are shown in Fig. 6. Unlike the spherical shape of the droplet, the meniscus inside the channel has a complicated shape since θ_{Ch} and θ_{EW} are not equal. Therefore, to obtain the meniscus pressure, an analysis of the surface tension forces acting on the advancing WLs in the channel is utilized. The effect of the electrostatic force is taken into account by considering a reduced θ_{EW} at the bottom of the channel due to EWOD.

The liquid meniscus in the channel is not spherical, yet due to a uniform Laplace pressure in the liquid, the sum of

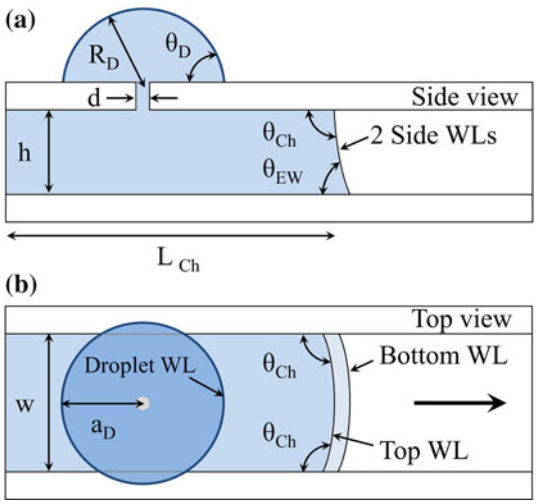

Fig. 5 Analytical model physical parameters defined on **a** *side view* of the micropump and **b** *top view* of the micropump

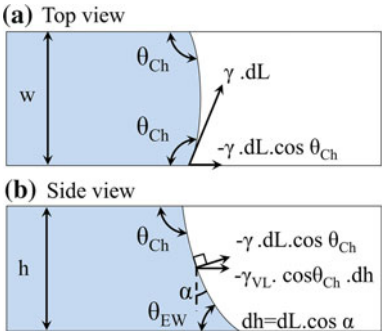

Fig. 6 Surface tension force exerted at the meniscus WL on the channel side wall **a** *top view* of the channel with a width of w. Differential length of the WL on the side wall is dL **b** *side view* of the channel with a height of h

the inverse of the two radii of curvatures ($1/R_1 + 1/R_2$) should be similar at all points on the meniscus. Except for the cases with a high symmetry, such as a square or rectangular channel with equal contact angles on all the channel walls (Hosokawa et al. 1999) and a confined droplet at equilibrium between two plates with equal contact angles (Schertzer et al. 2009), computational methods have been used to find the meniscus pressure (Zeng and Korsmeyer 2004). Nevertheless, it is possible to calculate the pressure of the meniscus inside a rectangular channel for a general case (different contact angles on the channel walls) without the need to calculate the surface curvature. An expression was derived for liquid meniscus pressure, P_M, based on the forces exerted on the meniscus WLs on the four walls of the channel. The parallel component of the surface tension force exerted on the liquid WL on the channel's side wall (Fig. 7a, b) was found to be $\gamma h \cos\theta_{Ch}$, where γ is the water surface tension (72 mN/m). Similarly, the parallel components of the surface tension forces exerted on the wetting lines on the top and bottom walls of the channel were found to be $\gamma w \cos\theta_{Ch}$ and $\gamma w \cos\theta_{EW}$, respectively. The meniscus pressure, P_M, is derived by dividing the sum of the surface tension forces parallel to the channel by the channel area:

$$P_M = (-\gamma/wh)[(2h + w)\cos\theta_{Ch} + w\cos\theta_{EW}] \quad (1)$$

The spherical droplet pressure, P_D, from Laplace pressure equation is $2\gamma/R_D$. The micropump driving pressure, P_{MP}, is the difference between P_M and P_D:

$$P_{MP} = \gamma \cdot ((2/R_D) + (\cos\theta_{Ch} \cdot (2h + w) + \cos\theta_{EW} \cdot w)/(hw)) \quad (2)$$

The total driving pressure in Eq. (2) should be equal to the viscous pressure loss in the channel, $h_f \rho g$, where ρ is liquid's density. The channel head loss, h_f, is obtained from the Darcy–Weisbach equation to be $fL_{eff}U_{Ch}^2/(2D_H \cdot g)$, in which f is the friction factor, L_{eff} is the effective liquid length in the channel (the sum of L_{Ch}, orifice length, and

other head losses), U_{Ch} is the liquid velocity in the channel, and D_H is the hydrodynamic diameter. D_H of the rectangular channel with a width, w, and a height, h, is equal to $2wh/(w + h)$. Reynolds number for the flow in the channel with an order of 1 mm/s is calculated to be ~ 0.1 using D_H. Thus, assuming a laminar flow in the microchannel, the friction factor will be $64/Re_{D_H}$. The relation between the micropump pressure, P_{MP}, and the liquid velocity in the channel, U_{Ch}, is expressed by:

$$U_{Ch} = P_{MP}/\left(8\,\mu\,L_{eff}\cdot(1/w+1/h)^2\right) \quad (3)$$

where μ is water viscosity (0.001 N.s/m^2). Bond number measures the relative strength of gravity with respect to surface tension and is defined as $g\rho L^2/\gamma$, where g is standard gravity and L is the characteristic length scale, for example, the droplet's radius or the height of the microchannel. Bond number for the droplet with an order of size of 1 mm is small (~ 0.1), and hence, the gravity is neglected throughout the rest of the analysis.

The capillary number is the ratio of viscous force to the surface tension force acting across the WL and is defined as $\mu U/\gamma$, where μ and γ are the liquid viscosity and surface tension, respectively, and U is the velocity of the WL. The capillary number is calculated to be much smaller than unity ($\sim 10^{-5}$) for water viscosity of 1 mPa.s and surface tension of 72 mN/m and an order of U of 1 mm/s. Thus, the surface tension force dominates the inertial force.

The dimensionless EW number represents the ratio of the electrostatic energy to the surface tension and is defined as $cV^2/(2\gamma)$, where c is the capacitance of the EWOD substrate and is calculated to be 10 μF/m^2 (Shabani and Cho 2012) and V is the applied DC voltage. EW number for the EWOD setup is calculated to be 1 for the applied DC voltage of 120 V. Therefore, for the range of the applied voltages, a substantial contact angle decrease could be achieved at the WL in the channel.

2.4 Flow rate analysis based on wetting-line energy and velocity effects

Equations (2) and (3) were implemented to develop an algorithm for flow rate analysis based on the WLE and WLV effects (Model 1 WLE and WLV). The continuity equation implies that the rate of the shrinkage of the input droplet is equal to the liquid flow rate in the channel. The initial θ_D for the input droplet was assumed to be equal to the relaxed advancing contact angle at zero voltage, which is 86° (Fig. 3b).

In phase I of the micropump, θ_D changes from 86° to 80° with a constant droplet wetted area due to the pinning. In phase II, in which droplet's WL is receding, data from Fig. 4b are used to estimate θ_D for the receding WL of the droplet. Data in Fig. 4c are used to find θ_{Ch}, in phases I and II for the advancing WL in the channel. The liquid contact angle on the bottom of the channel, θ_{EW}, was obtained by the flow rate analysis.

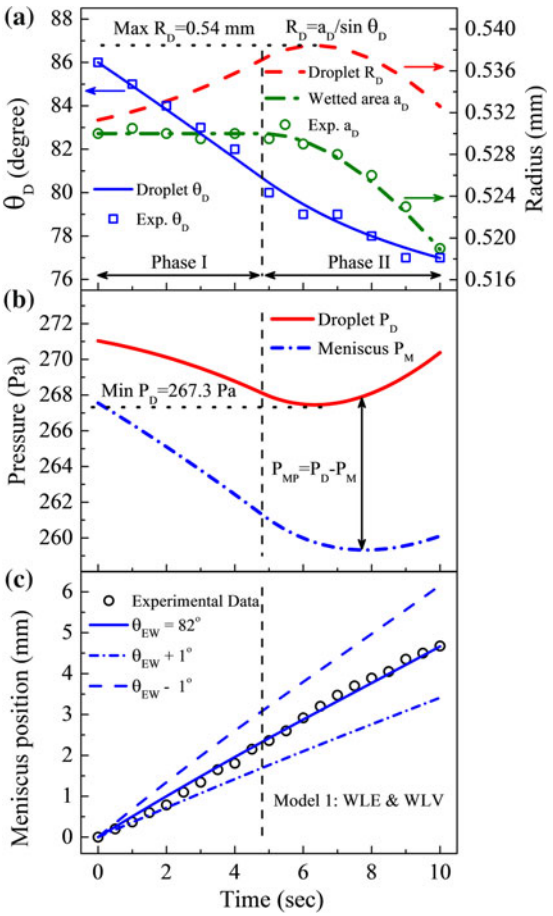

Fig. 7 Model 1 WLE and WLV numerical values for **a** droplet's θ_D, a_D, and R_D versus time. Measurement data for θ_D and a_D are *plotted* **b** P_D and P_M versus time **c** meniscus position versus time. *Circles* are the data and *solid line* is the best fit to the data. *Dashed line* and *dot-dashed line* show the effect of a small change in θ_{EW} (±1°) on the convergence of the fit

Since on the one hand θ_{Ch} is a function of U_{Ch} (Fig. 4c) and on the other hand U_{Ch} is a function of θ_{Ch} [Eqs. (2) and (3)], an implicit approach was used here to calculate θ_{Ch} based on the self-consistency of the results. In each time step a guess value for θ_{Ch} was chosen, and then U_{Ch} was calculated from Eqs. (2) and (3). However, it should be noted that the assumed θ_{Ch} and the value obtained for U_{Ch} should be in agreement with the data shown in Fig. 4c. Therefore, the initial value for θ_{Ch} was modified until the calculated U_{Ch} shows a good agreement with the experimental data.

Figure 7 shows an excellent agreement between the measurement and numerical values obtained by model 1 (WLE and WLV), using θ_{EW} of 82° for an initial droplet size, $2a_D$, of 1.06 mm. Figure 7a shows the experimental and calculated values for the radius of droplet wetted area,

a_D, and droplet contact angle, θ_D, and also calculated values for droplet radius of curvature, R_D, versus time. The transition from phase I to phase II is marked with vertical dashed line at 4.8 s. In Fig. 7b, P_D and P_M are shown as the droplet is driven into the channel. The droplet pressure decreases in phase I from 271 Pa to a minimum of 267.3 Pa and increases again in phase II. However, the driving pressure which is the difference between P_D and P_M increases monotonically to overcome the increasing viscous loss. In Fig. 7c the estimated liquid meniscus position versus time is compared to the measurement data. The calculated data exhibit the linear behavior as the experimental data.

In phase I of micropump operation, θ_D is reduced (Fig. 7a), resulting in an increase in R_D and subsequently a decrease in the droplet pressure (Fig. 7b). However, phase II is more complex since both a_D and θ_D are changing (Fig. 7a). Therefore, the change in P_D and P_M is non-monotonic in phase II. Interestingly, the meniscus pressure seems to follow the droplet pressure, and therefore, the driving pressure of the pump (the difference between P_D and P_M) remains small over time (Fig. 7b).

This phenomenon is the underlying reason for the constant flow reported for this micropump. Since the size of the meniscus in the *microscale* channel is much smaller than the droplet's free surface, small changes in θ_{Ch} ($\pm 0.1°$) could change P_M sufficiently to compensate for the change in P_D (Fig. 7b). Therefore, the variation in micropump's pressure induced by the shrinking input droplet would result in small variation in meniscus contact angle. Since θ_{Ch} and U_{Ch} are linked through WLV effect, such small changes in θ_{Ch} also imply negligible changes in the liquid velocity in the channel which explains why the liquid velocity and therefore the flow rate remain nearly constant. The dynamic contact angle of the meniscus in the channel is the dominant factor determining the flow rate according to this analysis.

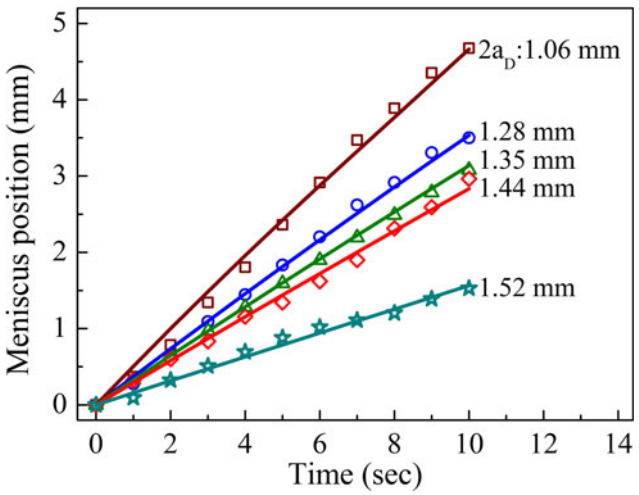

Fig. 8 Model 1 WLE and WLV predicting the meniscus position versus time for different diameters of the droplet wetted area, $2a_D$. *Markers* are measurement data and *solid lines* are the best fits to the data

2.4.1 *Droplet size effect on flow rate*

The meniscus velocity in the channel is higher for smaller sizes of the droplet (Shabani and Cho 2011). The numerical values obtained by model 1 WLE and WLV are in good agreement with the experimental data for the meniscus position in the micropump's channel for different sizes of the droplet (Fig. 8). The analytical fits to the data follow a similar linear behavior as the experimental data.

2.4.2 *EWOD voltage effect on flow rate*

Micrographs of a droplet with advancing and receding WLs show the EWOD voltage effect on the WL pinning and the contact angle hysteresis (Fig. 9a). DI water was injected (drawn) through a needle, at a very low flow rate to form a droplet with advancing (receding) WL. A high-gauge needle (30G) was used to minimize the distortion in

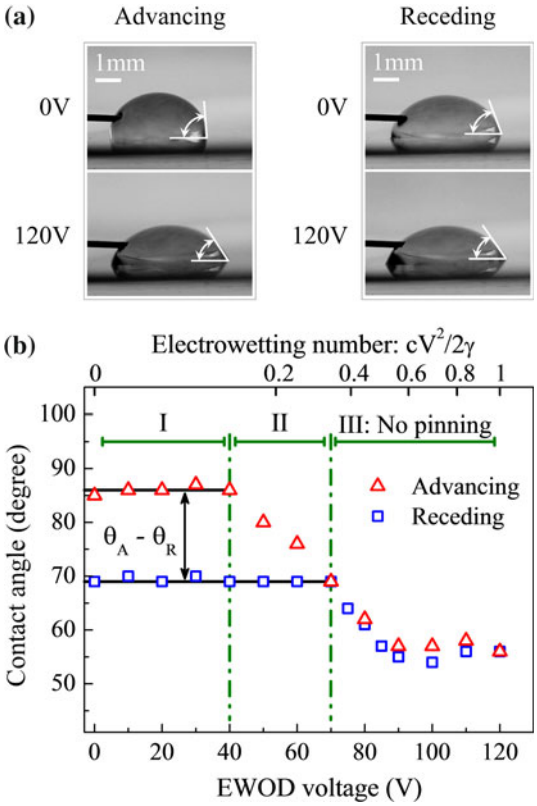

Fig. 9 WLE effect competing with EWOD. **a** Droplet advancing and receding contact angles decrease by increasing the voltage from 0 to 120 V. Also, the difference between advancing and receding contact angles decreases at higher voltages. **b** Advancing and receding contact angles at different voltages (EW numbers)

the droplet shape. The needle was also used to apply a DC voltage to the droplet (Fig. 2b). To avoid the WLV effect, ample time was given to the droplet for relaxation.

The advancing (receding) θ_D was measured for different DC voltages between 0 and 120 V (Fig. 9b). For voltages less than 40 V the advancing contact angle is not affected by EWOD ($\theta_A \sim 86°$), while above that, the contact angle is decreased. However, for voltages above 90 V, the contact angle reaches its lowest value and saturates at $\theta_A \sim 56°$ (Brassard et al. 2008). A very similar pattern was observed for the receding contact angle, only with a larger onset voltage for EWOD to affect the contact angle (70 V). Such transition region between the highest and lowest contact angles by increasing the applied voltage has been also reported previously (Berthier et al. 2007). Interestingly, the WL pinning effect (the difference between the advancing and receding contact angles, θ_A–θ_R) is noticeable at voltages below 40 V (region I in Fig. 9b), while at voltages above 70 V there is no significant pinning effect (region III in Fig. 9b). There is also a transition region in which the pinning effect decreases gradually since only θ_A is affected by EWOD (region II in Fig. 9b).

It has been reported that for a DC voltage, the hysteresis is essentially voltage independent (Li and Mugele 2008) while in this study a decrease in the pinning effect was observed for voltages above 40 V (region II and III in Fig. 9b). This is due to the fact that there are several major differences between the experimental setups used in these two studies, such as the working liquid, insulating material and its thickness, and also different range of EW numbers (Fig. 9b).

In a second set of experiments, the low pinning regime (region III in Fig. 9b) was more closely studied by changing the micropump working voltage from 60 to 100 V. The EWOD-based micropump depicted in Fig. 1 was used as the test setup. An input droplet with an initial size of 1 mm was used for the measurements at different voltages. By applying the voltage, the droplet was driven into the channel. The liquid meniscus position in the channel was measured versus time for each voltage (Fig. 10a, b).

Interestingly, the flow rate at low voltages (60 V < V<100 V) is completely nonlinear (Fig. 10b), and it changes drastically at different meniscus positions inside the channel. This behavior is due to surface defects (located randomly inside the channel) which increase the contact angle and therefore reduce the flow rate. The influence of such defects seems to be lessened for higher voltages (e.g., at 100 V), and hence, such voltages are needed as the working voltage of the micropump, if a constant flow rate is desired.

Since the location of surface defects cannot be measured inside the channel, any attempt to model such a complex system could only aim to obtain the effective average flow rates but not the local values. Figure 10b shows the experimental and calculated meniscus positions versus time at different voltages. A better agreement is obtained between the calculated and the measured data when the EWOD voltage is high enough to suppress the effect of local surface defects on dynamic contact angle. The calculated θ_{EW} for different voltages (Fig. 10c) is higher than the relaxed advancing contact angle at a similar voltage (Fig. 9b). This is in agreement with the concept of dynamic contact angle which shows larger values for larger advancing meniscus velocities.

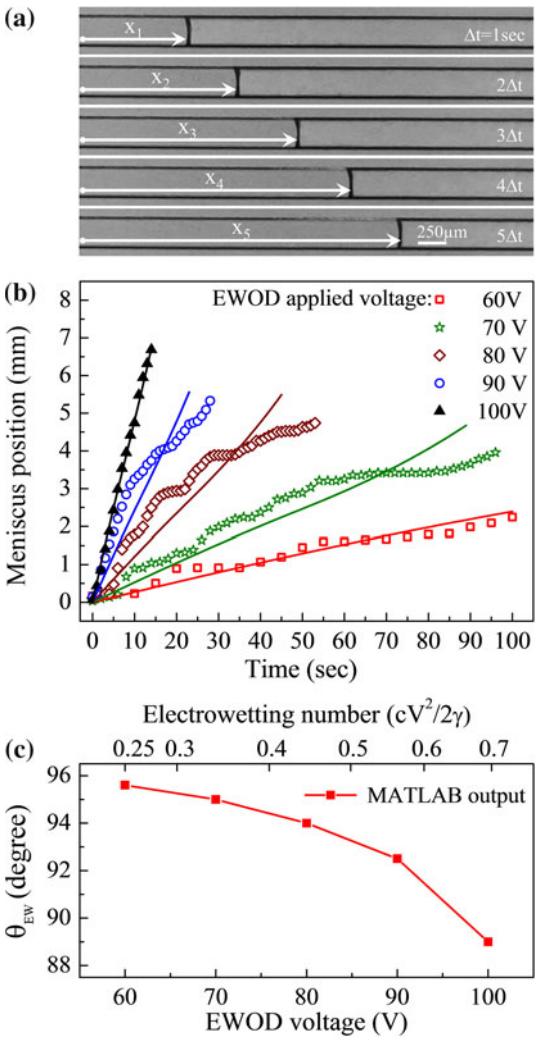

Fig. 10 EWOD voltage effect on flow rate. **a** *Top-view* pictures of the micropump's channel taken in every second show the advancing meniscus at 100 V. **b** Model 1 WLE and WLV predicting meniscus position versus time for different voltages. *Markers* are measured data and *solid lines* are best fits to data. **c** Numerical values for θ_{EW} versus EWOD voltage

Table 1 Experimental assumptions and dynamic contact angles used in models 1–3

	Assumptions	θ_D (phase I)	θ_D (phase II)	θ_{Ch}	θ_{EW}
Model 1	Comprehensive (WLE and WLV)	86° → 80° (a_D CONST)	Data in Fig. 4b	Data in Fig. 4c	82°
Model 2	Young–Tadmor (only WLE)	86° → 80° (a_D CONST)	80°	100°	88°
Model 3	Young's equation (Young contact angle)	86°	86°	86°	109°

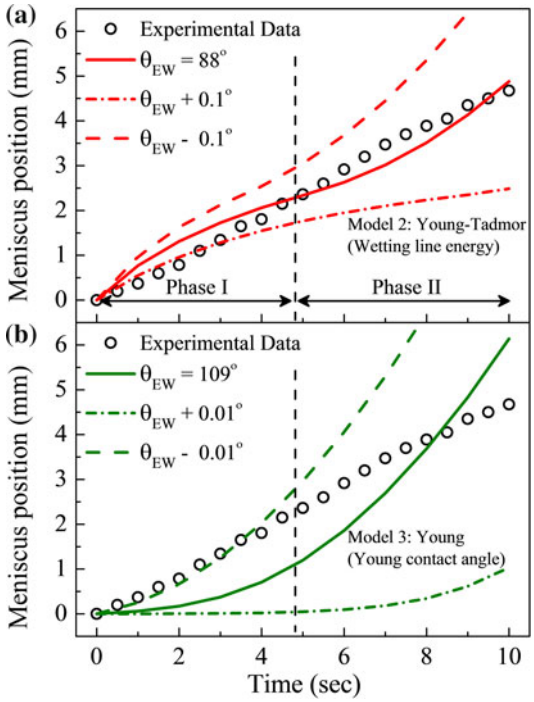

Fig. 11 Meniscus position versus time for **a** model 2 (Young–Tadmor) and **b** model 3(Young). *Circles* are measurement data and *solid lines* are the best fits to the data. *Dashed lines* and *dot-dashed lines* show the effect of a small change in θ_{EW} on the convergence of the fit

2.5 Comparison with wetting-line energy model and Young contact angle model

In order to highlight the importance of considering the WLE and WLV effects on the moving WL, two further models (models 2 and 3) were developed and compared to the comprehensive model 1 shown in the previous section. Model 2 is based on the WLE effect (Tadmor 2004) and does not include the WLV effect on contact angle (model 2: Young–Tadmor). In model 3, neither the pinning effect nor the WLV effect was considered and the contact angle was assumed to be equal to the equilibrium Young contact angle (model 3: Young). The assumptions and the contact angle values for each model are reported in Table 1 for comparison.

The numerical values for the liquid meniscus position in the channel for an initial diameter of the droplet wetted area, $2a_D$, of 1.06 mm are plotted for model 1 (Fig. 7c) and for models 2 and 3 (Fig. 11a, b, respectively). The values obtained for the θ_{EW}, for models 1–3, are tabulated in Table 1. In model 3 based on equilibrium Young contact angle (Fig. 11b), a large gap exists between the measured and the predicted flow rate (Walker et al. 2009; Walker and Shapiro 2006). Model 2 provides a better fit to measured data (Fig. 11a) as compared to the model 3 by taking into account the pinning effect. The predicted flow is significantly improved by including the WLV effect in model 1 (Fig. 7c). The sensitivity of the calculations to θ_{EW} is also investigated. In model 1, if θ_{EW} is changed by 1°, the estimated flow in the channel will slightly vary, while maintaining its linear behavior (Fig. 7c), unlike models 2 and 3 which are very sensitive to small changes in θ_{EW} (Fig. 11b, c). This also shows the accuracy of the estimated θ_{EW} by model 1. It is expected that the contact angle is reduced at the bottom of the channel due to EWOD (Lippmann 1875). The value obtained for θ_{EW} (82°) is reasonable since it should be smaller than θ_{Ch} with a value of 104°, due to EWOD.

Although the comprehensive model 1 utilizes several nonlinear experimental equations, its estimation of flow rate provides an excellent agreement with the observed constant flow rate. Such comparison shows the importance of taking both the WLE and the WLV effects into account for an accurate and realistic flow rate analysis.

3 Conclusions

A systematic approach was utilized to show the importance of taking account of the dynamic contact angle and explain the behavior of microfluidic devices that involve a moving WL. The microfluidic device used in this study is an EWOD micropump which exhibits dynamic contact angles both in the source droplet and in the meniscus inside the microchannel. The WL-related phenomena were comprehensively studied, since the device performance was strongly affected by contact angle hysteresis, WLV effect, and EWOD.

Some of the major experimental findings were as follows: (1) a mode switch in micropump operation originates from the contact angle hysteresis; (2) the dynamic contact angle based on the magnitude and direction of WLV in a microscale channel is responsible for constant flow rate; (3) EWOD reduces the contact angle for voltages

larger than an onset voltage and its effect saturates at higher voltages, and (4) EWOD could reduce the pinning effect using DC voltages.

A flow rate analysis of the EWOD micropump, based on the continuity and energy equations by implementing the aforementioned experimental observations, was conducted. The predicted flow rate was in excellent agreement with the measured constant flow rate of the micropump.

The lower pinning effect at higher working voltages leads to a relatively higher and constant flow measured in the channel. The effect of EWOD voltage on the flow rate was modeled, and the numerical values obtained by comprehensive model, based on WLE and WLV effects, for the dynamic θ_{EW} were verified against the relaxed advancing contact angles at a similar voltage.

Simpler models, based on Young's equation (equilibrium Young contact angle) and Young–Tadmor equation (incorporating the pinning effect on contact angle) were developed for comparison. They show disagreement between the numerical and measured flow rates, and predict an unphysical behavior for the system. Such examples demonstrate the importance of inclusion of the aforementioned wetting-line energy and wetting-line velocity effects to accurately model the flow rate, in particular for the micropump investigated in our study, and in general for any devices utilizing the Laplace pressure gradient.

Acknowledgments This work was supported by NSF (ECCS 0901503 and ECCS 1102280) and by KOSEF (WCU R32-2008-000-10124-0).

References

Ahmadi A, Holzman JF, Najjaran H, Hoorfar M (2010) Electrohydrodynamic modeling of microdroplet transient dynamics in electrocapillary-based digital microfluidic devices. Microfluid Nanofluid 10(5):1019–1032. doi:10.1007/s10404-010-0731-z

Annapragada SR, Dash S, Garimella SV, Murthy JY (2011) Dynamics of droplet motion under electrowetting actuation. Langmuir 27(13):8198–8204. doi:10.1021/La201322b

Bahadur V, Garimella SV (2006) An energy-based model for electrowetting-induced droplet actuation. J Micromech Microeng 16(8):1494–1503. doi:10.1088/0960-1317/16/8/009

Baviere R, Boutet J, Fouillet Y (2008) Dynamics of droplet transport induced by electrowetting actuation. Microfluid Nanofluid 4(4):287–294. doi:10.1007/s10404-007-0173-4

Berthier E, Beebe DJ (2007) Flow rate analysis of a surface tension driven passive micropump. Lab Chip 7(11):1475–1478

Berthier J, Dubois P, Clementz P, Claustre P, Peponnet C, Fouillet Y (2007) Actuation potentials and capillary forces in electrowetting based microsystems. Sens Actuators, A 134(2):471–479. doi:10.1016/j.sna.2006.04.050

Blake TD (2006) The physics of moving wetting lines. J Colloid Interface Sci 299(1):1–13

Blake TD, De Coninck J (2002) The influence of solid–liquid interactions on dynamic wetting. Adv Colloid Interface Sci 96(1–3):21–36. doi:10.1016/s0001-8686(01)00073-2

Brassard D, Malic L, Normandin F, Tabrizian M, Veres T (2008) Water-oil core-shell droplets for electrowetting-based digital microfluidic devices. Lab Chip 8:1342–1349

Chen JH, Hsieh WH (2006) Electrowetting-induced capillary flow in a parallel-plate channel. J Colloid Interface Sci 296(1):276–283. doi:10.1016/j.jcis.2005.08.048

Dussan VEB (1979) On the spreading of liquids on solid surfaces: static and dynamic contact lines. Annu Rev Fluid Mech 11(1):371–400. doi:10.1146/annurev.fl.11.010179.002103

Hosokawa K, Fujii T, Endo I (1999) Droplet-based nano/picoliter mixer using hydrophobic microcapillary vent. In: Micro electro mechanical systems, MEMS '99. Twelfth IEEE international conference on 17–21 Jan 1999, pp 388–393

Huh C, Scriven LE (1971) Hydrodynamic model of steady movement of a solid/liquid/fluid contact line. J Colloid Interface Sci 35(1):85–101. doi:10.1016/0021-9797(71)90188-3

Jang L-S, Lin G-H, Lin Y-L, Hsu C-Y, Kan W-H, Chen C-H (2007) Simulation and experimentation of a microfluidic device based on electrowetting on dielectric. Biomed Microdevices 9(6):777–786. doi:10.1007/s10544-007-9089-8

Keshavarz-Motamed Z, Kadem L, Dolatabadi A (2009) Effects of dynamic contact angle on numerical modeling of electrowetting in parallel plate microchannels. Microfluid Nanofluid 8(1):47–56. doi:10.1007/s10404-009-0460-3

Li F, Mugele F (2008) How to make sticky surfaces slippery: contact angle hysteresis in electrowetting with alternating voltage. Appl Phys Lett 92 (24). doi:10.1063/1.2945803

Lienemann J, Greiner A, Korvink JG (2006) Modeling, simulation, and optimization of electrowetting. IEEE Trans Comput Aided Des Integr Circuits Syst 25(2):234–247. doi:10.1109/Tcad.2005.855890

Lippmann G (1875) Relation entre les phenomenes electriques et capillaires. Ann Chim Phys 5:494–549

Lu H-W, Glasner K, Bertozzi AL, Kim C-J (2007) A diffuse-interface model for electrowetting drops in a Hele-Shaw cell. J Fluid Mech 590:411–435. doi:10.1017/S0022112007008154

Mugele F, Baret JC (2005) Electrowetting: from basics to applications. J Phys Condens Matter 17(28):R705–R774. doi:10.1088/0953-8984/17/28/R01

Nelson WC, Sen P, Kim C-JC (2011) Dynamic contact angles and hysteresis under electrowetting-on-dielectric. Langmuir 27(16):10319–10326. doi:10.1021/la2018083

Pai P-L (1987) Material characteristics of spin-on glasses for interlayer dielectric applications. J Electrochem Soc 134(11):2829. doi:10.1149/1.2100297

Quinn A, Sedev R, Ralston J (2005) Contact angle saturation in electrowetting. J Phys Chem B 109(13):6268–6275. doi:10.1021/jp040478f

Ren H, Fair RB, Pollack MG, Shaughnessy EJ (2002) Dynamics of electro-wetting droplet transport. Sens Actuators B Chem 87(1):201–206

Schertzer MJ, Gubarenko SI, Ben Mrad R, Sullivan PE (2009) An empirically validated model of the pressure within a droplet confined between plates at equilibrium for low Bond numbers. Exp Fluids 48(5):851–862. doi:10.1007/s00348-009-0773-8

Schertzer MJ, Gubarenko SI, Ben-Mrad R, Sullivan PE (2010) An empirically validated analytical model of droplet dynamics in electrowetting on dielectric devices. Langmuir 26(24):19230–19238. doi:10.1021/La103702t

Sen P, Kim CJ (2009) Capillary spreading dynamics of electrowetted sessile droplets in air. Langmuir 25(8):4302–4305. doi:10.1021/La900077u

Shabani R, Cho HJ (2011) A micropump controlled by EWOD: wetting line energy and velocity effects. Lab Chip 11(20):3401–3403. doi:10.1039/C1lc20440h

Shabani R, Cho HJ (2012) Active surface tension driven micropump using droplet/meniscus pressure gradient. Sens Actuators B Chem, doi:10.1016/j.snb.2012.05.058

Shikhmurzaev YD (2006) Singularities at the moving contact line. Mathematical, physical and computational aspects. Physica D 217(2):121–133

Tadmor R (2004) Line energy and the relation between advancing, receding, and young contact angles. Langmuir 20(18):7659–7664. doi:10.1021/la049410h

Tanner LH (1979) The spreading of silicone oil drops on horizontal surfaces. J Phys D Appl Phys 12(9):1473–1484. doi:10.1088/0022-3727/12/9/009

Walker SW, Shapiro B (2006) Modeling the fluid dynamics of electrowetting on dielectric (EWOD). J Microelectromech Syst 15:986–1000

Walker SW, Shapiro B, Nochetto RH (2009) Electrowetting with contact line pinning: computational modeling and comparisons with experiments. Phys Fluids 21(10):102103

Wang YL, Liu C, Chang ST, Tsai MS, Feng MS, Tseng WT (1997) Chemical-mechanical polishing of low-dielectric-constant spin-on-glasses: film chemistries, slurry formulation and polish selectivity. Thin Solid Films 308:550–554. doi:10.1016/S0040-6090(97)00491-4

Young T (1805) An essay on the cohesion of fluids. Philos Trans R Soc Lond 95:65–87

Zeng J, Korsmeyer T (2004) Principles of droplet electrohydrodynamics for lab-on-a-chip. Lab Chip 4:265–277